2018 Annual American Control Conference (ACC)
June 27–29, 2018. Wisconsin Center, Milwaukee, USA

System Identification of a Discrete Repetitive Process Model for Electrohydrodynamic Jet Printing

Zhi Wang[1] *Student Member*, Patrick M. Sammons[2] *Member*, Christopher P. Pannier[2] *Student Member*,
Kira Barton[2] *Member*, and David J. Hoelzle[3] *Member*

Abstract— **Microscale additive manufacturing processes have a great potential to manufacture microscale sensors and devices in a layer-to-layer fashion with freeform control of device architecture. However, the layer-to-layer dynamics in microscale additive manufacturing are not well understood. This manuscript investigates layer-to-layer dynamics from a system identification perspective. This work defines a class of input signals, system identification algorithm for microscale additive manufacturing modeled as a discrete repetitive system, and the experimental protocol to empirically the plant model and validate the model for a different input signal. A case study applied to the microscale additive manufacturing process electrohydrodynamic jet printing demonstrates that the identified model from a training set is extensible to a validation data set, with less than 4% error between the system identification of the training and validation data sets.**

I. INTRODUCTION

Additive manufacturing (AM) systems technology have attracted significant attention in recent years. In AM, a 3D object model is sliced into multiple layers in a computer program and the AM system selectively adds material on each layer on top of the existing material [1]. AM has advantages over traditional manufacturing techniques, including: 1) the ability to fabricate complex structures that are not feasible by traditional manufacturing techniques; 2) rapid prototyping of new designs; 3) reduced material waste; 4) meeting custom manufacturing requirements; and 5) does not expensive tooling, hence reducing cost.

The majority of the applications of AM are in the macroscale. However, AM techniques have been expanded to the microscale, termed Microscale-Additive Manufacturing (μ-AM). One of the representative μ-AM technologies is electrohydrodynamic jet (e-jet) printing. In e-jet, a voltage difference is applied between a conductive nozzle and a conductive printing substrate, pulling the ink material at the nozzle tip from spherical meniscus to a conical shape and then ejecting the ink drop onto the substrate. Structures are fabricated by coordinate nozzle position and droplet ejection. E-jet is advantageous because it can fabricate objects in microscale and nanoscale [2] because the electric field deforms a spherical droplet into a cone, hence reducing the fundamental droplet size and thus resolution; resolution is on a comparable lengthscale to lithographic micromachining, making e-jet a compelling technology for fabrication of biological micro-assays [3], charge printing for self assembly [4], electronics [5], [6] and many others [7], [8].

Current μ-AM techniques primarily fabricate objects in 2D [2], [9], [10]. However, the real potential of μ-AM is the ability to fabricate in 3D. In contrast to 2D μ-AM, in 3D μ-AM, once a base layer of material has been deposited, subsequent layers build upon each other, creating dynamics in the layer-to-layer domain [11], [12]. Ultimately, μ-AM control methods like those published by the authors [13], [14] and others [12] will be applied to multi-layer, multi-material fabrication; to realize stable feedback loops, we must have an accurate model of the in-layer and layer-to-layer dynamics. The authors' previous work [13], [14] demonstrate 2D μ-AM regulated autonomously with iterative learning control, while this manuscript will demonstrate layer-to-layer system identification.

In this manuscript, the in-layer and layer-to-layer dynamics of a 3D μ-AM system are formulated as a spatial, discrete repetitive process. We define and demonstrate an empirical method to obtain a model, using established tools from system identification. Section II defines the discrete repetitive system model posed to capture in-layer and layer-to-layer dynamics. Section III defines the system identification method, including the definition of 2D pseudo random binary sequence (PRBS) input signals as the system excitation and μ-AM appropriate constraints on the algorithm. Section IV defines the specific μ-AM system used for a case study, electrohydrodynamic jet (e-jet) printing, and the specific of system identification application. Section V presents system identification results and then Section VI provides conclusions and future directions.

II. DISCRETE REPETITIVE SYSTEM MODEL

On each layer in the layer-to-layer sequence of material addition in μ-AM, material is selectively added at a given position $\{x, y\}$. The accumulated topography on layer $j+1$ at $\{x, y\}$, $g_{j+1}(x, y)$, is the sum of the previously accumulated layers of material, $g_j(x, y)$ and the newly added material, $H_f f_{j+1}$ (Fig. 1). While material addition is commanded at position $\{x, y\}$, there is also material spill-over from material added at adjacent positions (e.g. $\{x-1, y\}$). Note that in this study, as with previous work from the authors [13], [14], we

---

*This draft manuscript was submitted for review on February 26, 2018. This work was supported in part by NSF Awards CMMI-1434660, CMMI-1434693, CMMI-1727894, and DGE 1256260.

[1] Wang is with the Department of Aerospace and Mechanical Engineering at the University of Notre Dame, Notre Dame, IN 46556 USA `zwang10@nd.edu`

[2] Sammons, Pannier, and Barton are with the Department of Mechanical Engineering at the University of Michigan, Ann Arbor, MI 48109 USA `bartonkl@umich.edu`

[3] Hoelzle is with the Department of Mechanical and Aerospace Engineering at the Ohio State University, Columbus, OH 43210 USA `hoelzle.1@osu.edu`

978-1-5386-5428-6/$31.00 ©2018 AACC

assume that temporal dynamics are not observable with the sensors we used and thus temporal dynamics are ignored.

This sequence of material addition is naturally a discrete repetitive process (DRP), so it can be abstractly modeled by the general DRP formulation in operator form (Fig. 2)

$$g_{j+1} = H_f f_{j+1} + H_g g_j. \tag{1}$$

where H_g denotes the material spill-over to adjacent coordinates caused by the previously accumulated topography, and w is the layer shift operator: $wg_j = g_{j+1}$.

Remark 1: We expect that H_g is a pure integrator where previous layers simply add to the cumulative layer height. In agreement with systems identification practice, we do not suppose a model for H_g and we evaluate whether or not our expectation of a pure integrator is confirmed.

A. 2D convolution representation

Spatially-invariant forms of the operators H_f and H_g, (1) can be rewritten as a discrete, 2D convolution

$$\begin{aligned} g_{j+1}(x,y) &= \left(f_{j+1} * h_f\right)(x,y) + \left(g_j * h_g\right)(x,y) \\ &= \sum_{u=0}^{M-1}\sum_{v=0}^{N-1} f_{j+1}(u,v) h_f(x-u, y-v) \\ &+ \sum_{u=0}^{M-1}\sum_{v=0}^{N-1} g_j(u,v) h_g(x-u, y-v), \end{aligned} \tag{2}$$

where h_f is the discrete impulse response to the current layer input and h_g is the discrete impulse response to the previous layer output. f_{j+1} and $g_{(\cdot)}$ are discrete functions at $x = 0, 1, \ldots, M-1$ and $y = 0, 1, \ldots, N-1$.

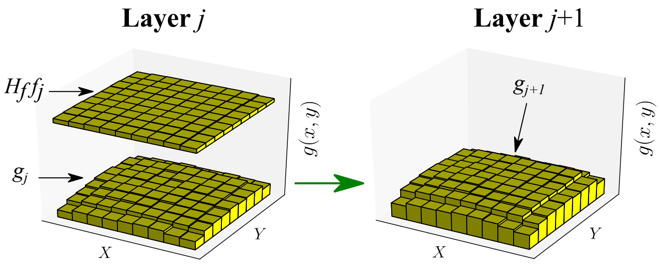

Fig. 1. Schematic of material accumulation in μ-AM. The accumulated material height, g_{j+1}, at layer $j+1$ is a function of the underlying material accumulation from previous layers, g_j, and the current layer material addition, $H_f f_j$.

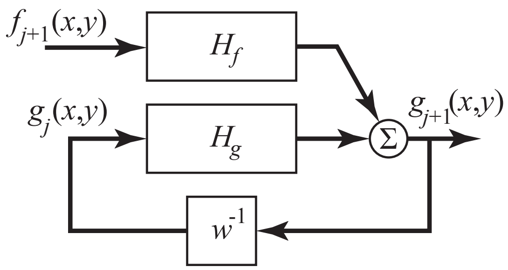

Fig. 2. Operator model for a spatial discrete repetitive system.

B. Lifted-domain representation

To leverage standard temporal-domain system identification algorithms, the system representation in (2) can be transformed to the lifted-form

$$\mathbf{g}_{j+1} = \mathbf{H_f} \mathbf{f}_{j+1} + \mathbf{H_g} \mathbf{g}_j, \tag{3}$$

where $\mathbf{f}_{j+1} = \mathcal{V}(f_{j+1}) \in \mathbb{R}^{MN\times 1}$ and $\mathbf{g}_{(\cdot)} = \mathcal{V}(g_{(\cdot)}) \in \mathbb{R}^{MN\times 1}$. The spatial dynamics matrices $\mathbf{H_f}, \mathbf{H_g} \in \mathbb{R}^{MN\times MN}$ are Block Circulant matrices with Circulant Blocks (BCCB) composed of the entries of the impulse response h_f, h_g as has been done before by the authors in [13]. $\mathcal{V}$ is the vectorization operator and $\mathcal{V}^{-1}$ is the matricization operator [15].

C. Finite Impulse Response (FIR) model

In practice for μ-AM systems, both h_f and h_g are finite horizon impulse response functions because there are two finite limits: 1) added material will spread to a finite extent; 2) the influence of the underlying topography has a finite extent. Therefore, the set of unknown parameters of h_f and h_g can be represented by an unknown parameter vector

$$\theta = \left[h_{f1}, h_{f2}, \ldots, h_{fm}, h_{g1}, h_{g2}, \ldots, h_{gn}\right]^T$$

where h_f is composed of m unknown parameters and h_g is composed of n unknown parameters. The values of m and n are determined by the dynamics of the system. The system dynamics in (3) can be rewritten as

$$\mathbf{g}_{j+1} = \Phi(\mathbf{f}_{j+1}, \mathbf{g}_j)\theta, \tag{4}$$

where $\Phi(\mathbf{f}_{j+1}, \mathbf{g}_j)$ is the transformation between θ and $\mathbf{g}_{j+1}$. In the general case, the vector θ can be written as

$$\theta = \begin{bmatrix} h_f(1-M, 1-N) \\ h_f(1-M, 2-N) \\ \vdots \\ h_f(1-M, N-1) \\ h_f(2-M, 1-N) \\ \vdots \\ h_f(2-M, N-1) \\ \vdots \\ h_f(M-1, N-1) \\ h_g(1-M, 1-N) \\ h_g(1-M, 2-N) \\ \vdots \\ h_g(1-M, N-1) \\ h_g(2-M, 1-N) \\ \vdots \\ h_g(2-M, N-1) \\ \vdots \\ h_g(M-1, N-1) \end{bmatrix}. \tag{5}$$

The corresponding $\Phi(\mathbf{f}_{j+1}, \mathbf{g}_j) \in \mathbb{R}^{MN\times 2(2M-1)(2N-1)}$ can be written as

$$
\begin{aligned}
&\Phi[u,v] \\
&= \left(1 - \lfloor \frac{v}{(2M-1)(2N-1)} \rfloor \right) \\
&\quad \times f_{j+1}\{\lfloor \frac{u}{N} \rfloor - \left(\lfloor \frac{v'}{2N-1} \rfloor + 1 - M \right), \\
&\quad (u \bmod N) - ((v' \bmod 2N-1) + 1 - N)\} \\
&\quad + \lfloor \frac{v}{(2M-1)(2N-1)} \rfloor \\
&\quad \times g_j\{\lfloor \frac{u}{N} \rfloor - \left(\lfloor \frac{v'}{2N-1} \rfloor + 1 - M \right), \\
&\quad (u \bmod N) - ((v' \bmod 2N-1) + 1 - N)\},
\end{aligned} \tag{6}
$$

where $u \in \{0, 1, 2, \ldots, MN - 1\}$ and $v \in \{0, 1, 2, \ldots, 2(2M-1)(2N-1) - 1\}$ are the row index and column index of $\Phi(\mathbf{f}_{j+1}, \mathbf{g}_j)$, respectively. The notation $\lfloor \cdot \rfloor$ denotes the floor function, and $v' = v \bmod (2M-1)(2N-1)$. The detailed derivation to obtain (6) is provided in Appendix I. The formulation in (6) is the general form. In practice, the formulation may be simplified based on the dynamics of the specific system. Sections IV-D and IV-E include an example of how to reduce the dimension and complexity of θ in practice.

III. SYSTEM IDENTIFICATION

System identification is a well-known tool to obtain a mathematical model of a dynamic system using empirical input and output signal data [16]. In this study, the purpose of system identification is to identify an estimate, $\hat{\theta}$, of the unknown parameters, θ in (4). Specifically, find $\hat{\theta}$ such that $\|\mathbf{g}_{j+1} - \Phi(\mathbf{f}_{j+1}, \mathbf{g}_j)\hat{\theta}\|_2^2$ is minimized, where $\mathbf{g}_{j+1}$ and Φ are known or measured from an experiment. This section details unique aspects of system identification for spatial discrete repetitive systems models for μ-AM.

A. Input signals

Multiple standard input signals used in temporal system identification can be adapted to 2D spatial layer-to-layer system identification. In this study, pseudo random binary sequence (PRBS) signals are adapted to 2D PRBS input signal matrices. PRBS signals are advantageous because they are deterministic, they possess frequency spectrum properties similar to white noise, and generate responses with better signal-to-noise ratios than white noise [17]. The construction details of a 1D PRBS can be easily found in many references such as [18], and are omitted in this manuscript. There are many standard software packages providing functions constructing 1D PRBS signals. Here, the built-in `idinput()` function in MATLAB is used. To identify 2D dynamics, 2D PRBS input signals are constructed using the method given in [18]. This manuscript provides the fundamental construction operations without mathematical proof. Readers interested in the mathematical details should reference [18].

The 2D PRBS signals can be constructed by folding a 1D PRBS signal. The operation begins with taking a number of the form $l = 2^{k_1 k_2} - 1$ such that $l_1 = 2^{k_1} - 1$ and $l_2 = l/l_1$ are relatively prime and greater than 1. Examples are

$$l = 15 = 2^4 - 1 \text{ with } k_1 = k_2 = 2, l_1 = 3, l_2 = 5$$
$$l = 63 = 2^6 - 1 \text{ with } k_1 = 3, k_2 = 2, l_1 = 7, l_2 = 9$$
$$l = 511 = 2^9 - 1 \text{ with } k_1 = 3, k_2 = 3, l_1 = 7, l_2 = 73.$$

The starting point is a 1D PRBS signal with the length of l. Fig. 3 shows an instructive example of folding a $l = 15$ 1D PRBS signal to a 3×5 2D PRBS signal.

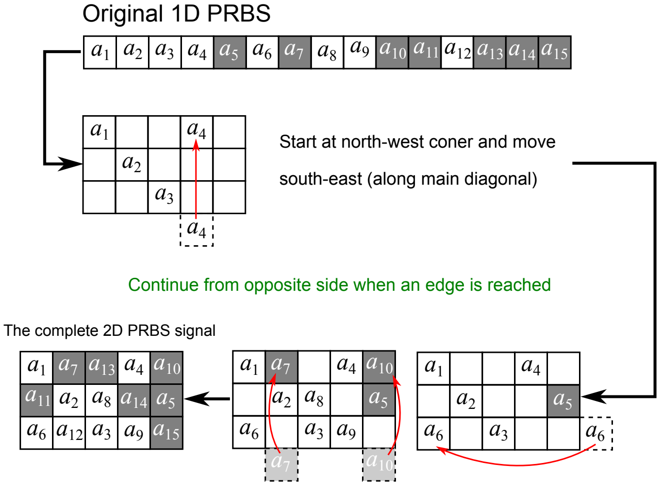

Fig. 3. Constructing a 2D PRBS signal from a 1D PRBS sequence.

B. System identification algorithm

The system identification problem is defined as

$$
\begin{aligned}
&\min_{\hat{\theta}} \|\mathbf{g}_{j+1} - \Phi(\mathbf{f}_{j+1}, \mathbf{g}_j)\hat{\theta}\|_2^2 \\
&\qquad\qquad \theta_{lower} \leqslant \hat{\theta} \leqslant \theta_{upper} \\
&\text{subject to: } \mathbf{A}_e \hat{\theta} = \mathbf{B}_e \\
&\qquad\qquad \mathbf{A}\hat{\theta} \geqslant \mathbf{B}
\end{aligned} \tag{7}
$$

where matrices $\{\mathbf{A}_e, \mathbf{B}_e\}$ and $\{\mathbf{A}, \mathbf{B}\}$ contain equality and inequality constraint parameters, respectively. The practical aspects of these constraints as they pertain to μ-AM are described in Section IV. Many standard software packages provide built-in solvers that can solve (7); here, we use the built-in solver `lsqlin()` in MATLAB.

IV. EXPERIMENT SETUP

System identification is performed on a μ-AM system housed in the Barton Research Group at the University of Michigan (Fig. 4a). This section provides details of the experimental system and the experiment procedure.

A. System description

The μ-AM system used in this study is an electrohydrodynamic jet (e-jet) printing system. The mechanism of material addition in e-jet is liquid-phase drop ejection where an electrostatic force from a voltage potential draws build material out of a microcapillary, with nozzle diameters orders

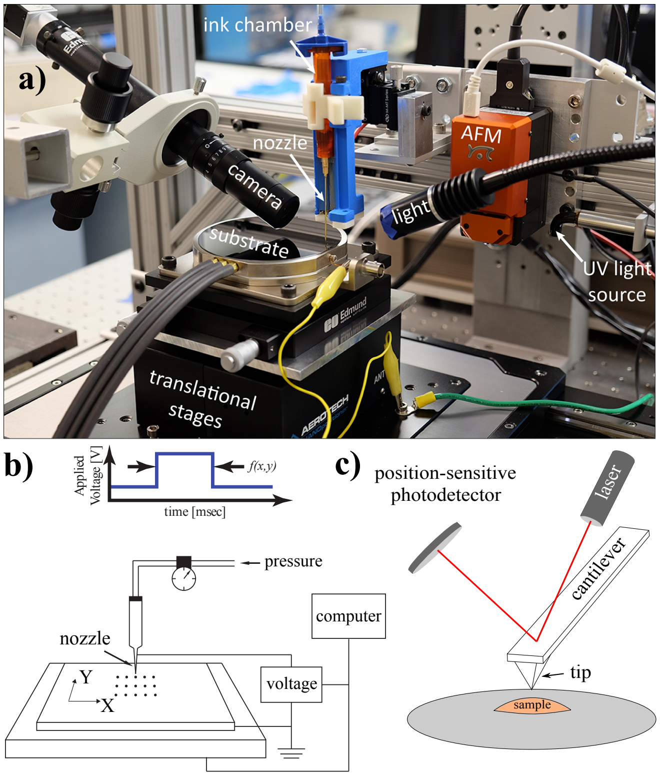

Fig. 4. μ-AM system in the Barton Research Group at the University of Michigan. a) A photograph presenting the components of the integrated system. b) Schematic of a standard e-jet system and the voltage pulse driving the drop ejection. c) Schematic of the AFM scan mechanism.

typically ranging from 100 nm to 10 μm, into a conical shape, termed a Taylor cone, and then ejects the material onto an underlying substrate. By coordinating the position of the nozzle with voltage actuation, structures with microscale features can be built from a variety of different function materials, including: silver- and gold-nanoparticles [19]–[22], polymers [23]–[25], and biological materials [3], [26], [27]. Readers interested in e-jet printing mechanism and other applications should reference [2], [28].

E-jet can be modeled in the context of the spatial discrete repetitive system in (4). The XY plane in Fig. 4b is discretized into a normal grid $x = 0, 1, \dots, M-1$ and $y = 0, 1, \dots, N-1$ with pitch p. At each grid coordinate (x, y), a voltage pulse is applied with pulse width $f_{j+1}(x, y)$, depositing an ink drop. The ink drop spreads to neighboring coordinates (e.g. $(x-1, y)$). The steady state topography height distribution is determined by the spatial dynamics h_f, input map, f_{j+1}, and the preexisting topography, g_j. For multi-layer fabrication, this process of ejecting drops at specific coordinates is repeated to produce the 3D object.

For the specific setup used in this study, the grid pitch is 5 μm. The inner diameter of the printing nozzle is 2 μm (World Precision Instruments TIP2TW1-L), and the standoff height between the nozzle and the substrate is 40 μm. An electrically grounded silicon wafer with a deposited layer of SiO_2 is used as the substrate. The topography is measured by an integrated atomic force microscope (AFM) that permits facile, registered measurements, as described in [14], [29]; here, we use a commercial tip-scanning AFM (Nanosurf NaniteAFM) with controller (Nanosurf C3000) and custom-written image processing algorithm. The ink material used is Loctite 3526, which is a UV curable adhesive. After deposition, the ink is cured by our UV curing station (Dymax BlueWave 200 Ver. 1.1).

B. System identification workflow

The aim of system identification for the discrete repetitive model (4) is to estimate the unknown parameter vector $\hat{\theta}$. There are unique considerations for the multi-layer structures printed by μ-AM. In particular, the surface energy of the substrate is different from the build material, meaning that a sessile drop will spread differently on the substrate than it will on a previous layer of the material. Therefore, system identification tests are performed on a pad of deposited ink. Accordingly, we use a two-layer deposition procedure (Fig. 5 and 6) and use only second layer input data for $\hat{\theta}$ estimation (algorithm in Section III-B). A first layer is deposited with pulse width map $\mathbf{f}_1$, scanned by AFM, and then processed, providing a base topography profile $\mathbf{g}_1$. Then a second layer is deposited on top of the first layer with pulse width map $\mathbf{f}_2$ and then scanned and processed to obtain $\mathbf{g}_2$. As presented in the workflow in Fig. 5, the workflow is repeated for 10 cycles with different f_1, f_2 maps to best represent the actual system responses to different inputs. Another 10 cycles with different f_1, f_2 maps are performed afterwards as validation. The input maps f_1, f_2 are constructed in the following manner:

$$f_j = d_i \bar{f}_j,\ i = 0, 1, \dots, 9 \text{ and } j = 1, 2 \tag{8}$$

where d_i is a pulse width scaling factor that spans the typical operating pulse width of the system and $\bar{f}_j$ is a 2D PRBS function template. To guarantee periodic boundary conditions for the identification of dynamics for the second layer, an augmented input $\tilde{f}_1$ is used to e-jet print the first layer. As shown in Fig. 6, $\tilde{f}_1$ is constructed by repeating f_1 in the XY plane and cropping a map 4 rows and 4 columns larger than f_1. Note that $\tilde{f}_1$ is not used for $\hat{\theta}$ estimation, which is given in Section III-B.

The model is validated using the same workflow as shown in Fig. 5, except using a set of validation PRBS templates $\bar{\bar{f}}_j$ for $j = 1, 2$. The identification model error and validation model error are quantitatively compared using the error metrics

$$\begin{aligned} E^{\text{exp}}_{\text{rms}} &= \sqrt{\frac{\left(\|\mathbf{g}_2^{\text{exp}} - \Phi(\mathbf{g}_1^{\text{exp}}, \mathbf{f}_2^{\text{exp}})\hat{\theta}\|_2\right)^2}{7 \times 9 \times 10}}, \\ E^{\text{val}}_{\text{rms}} &= \sqrt{\frac{\left(\|\mathbf{g}_2^{\text{val}} - \Phi(\mathbf{g}_1^{\text{val}}, \mathbf{f}_2^{\text{val}})\hat{\theta}\|_2\right)^2}{7 \times 9 \times 10}}, \end{aligned} \tag{9}$$

where $\hat{\theta}$ is the solution to problem (7). $\mathbf{f}_2^{\text{exp}}$ is the vectorized form of the input vectors in the 10 cycles of system

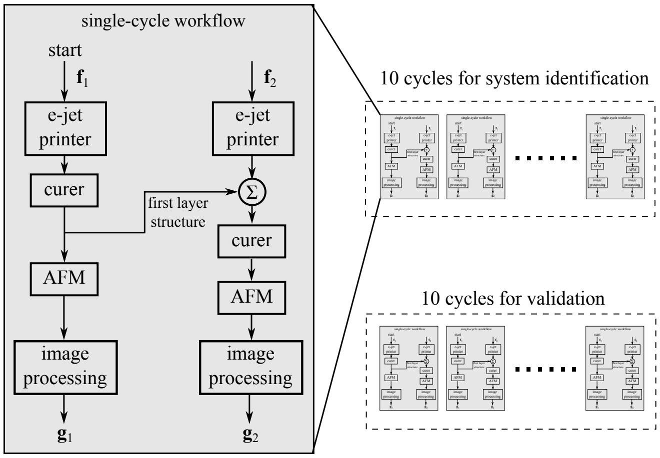

Fig. 5. Diagram of the experiment workflow.

identification runs:

$$\mathbf{f}_2^{\text{exp}} = \left[\mathcal{V}\left(d_0\bar{f}_2\right), \mathcal{V}\left(d_2\bar{f}_2\right), \ldots, \mathcal{V}\left(d_9\bar{f}_2\right)\right]^T.$$

$\mathbf{g}_{(\cdot)}^{\text{exp}}$ are the vectorized forms of the corresponding outputs in the system identification runs. $\mathbf{f}_2^{\text{val}}$ is the vectorized form of the input vectors in the 10 cycles of validation runs with different pulse width scaling factor, hencing different drop sizes:

$$\mathbf{f}_2^{\text{val}} = \left[\mathcal{V}\left(d_0\bar{\bar{f}}_2\right), \mathcal{V}\left(d_2\bar{\bar{f}}_2\right), \ldots, \mathcal{V}\left(d_9\bar{\bar{f}}_2\right)\right]^T.$$

$\mathbf{g}_{(\cdot)}^{\text{val}}$ are the vectorized forms of the corresponding outputs in the system identification runs.

C. Experimental Parameters

For both the identification and validation prints, the input map templates $\bar{f}_1, \bar{f}_2$ are 7×9 2D PRBS maps as shown in Fig. 7. The 2D PRBS matrices are generated from maximum length (63) 1D PRBS signals. The white pixels denote $\bar{f}_j = 1$, and the gray pixels denote $\bar{f}_j = 0.5$. The validation input template $\bar{\bar{f}}_2$ is formed identically to $\bar{f}_1$ via the approach illustrated in Fig. 3, except with a different initial condition for the 1D PRBS.

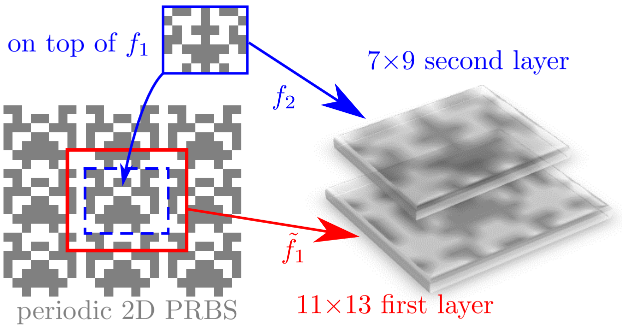

Fig. 6. Schematic of the two-layer printing experiment.

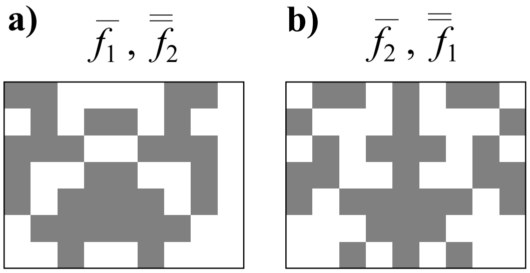

Fig. 7. 2D PRBS signals used to construct the input maps for the system identification experiments. Both a) and b) are constructed from length 63 1D PRBS signals under the manner in Fig. 3. The only difference between a) and b) is the initial condition of the 1D PRBS signals.

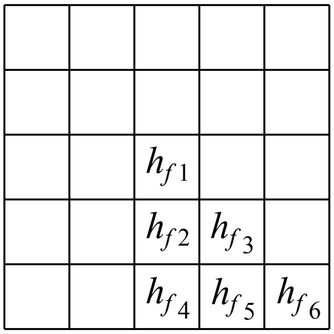

Fig. 8. From assumptions **A1** and **A2**, h_f is defined by six parameters $\{h_{f1}, h_{f2}, \ldots, h_{f6}\}$. h_g is similarly defined by six parameters $\{h_{g1}, h_{g2}, \ldots, h_{g6}\}$.

D. Model assumptions and corresponding constraints

The model makes four assumptions about the size and composition of h_f and h_g.

A1. Previous single-drop models indicate that the maximum spread of a drop to be less than 25 μm [30]. Using a $d = 5$ μm pitch, h_f and h_g take the form of 5×5 matrices.

A2. The e-jet printing system has discontinuous stage shifting operations in the experiment workflow. The substrate is stationary with respective to the nozzle when a drop is printed, then is shifted to the next coordinate for the next drop printing. Sessile drop theory predicts rotational symmetry for liquid drops [31], so h_f and h_g have center-inversion and 90-degree rotational symmetry so that the 25 elements of each of h_f and h_g are completely defined by six parameters each (Fig. 8).

A3. A sessile drop topography monotonically decreases from it center [31], so $h_{f1} \geq h_{f2} \geq \ldots \geq h_{f6}$.

A4. Material can only be added, so $h_{fi}, h_{gi} \geq 0$. Additionally, the layer-by-layer operator h_g conserves volume, so $1h_{g1} + 4h_{g2} + 4h_{g3} + 4h_{g4} + 8h_{g5} + 4h_{g6} = 1$.

E. Constraints

Assumptions **A1** and **A2** dictate the form of $\hat{\theta}$,

$$\hat{\theta} = \left[h_{f1}, h_{f2}, \ldots, h_{f6}, h_{g1}, h_{g2}, \ldots, h_{g6}\right]^T. \tag{10}$$

Assumption **A3** sets

$$\mathbf{A} = \begin{bmatrix} \mathbf{\Delta} & \mathbf{0}^{6\times 6} \\ \mathbf{0}^{6\times 6} & \mathbf{\Delta} \end{bmatrix}; \mathbf{B} = \mathbf{0}^{12\times 1} \tag{11}$$

where the difference matrix

$$\mathbf{\Delta} = \begin{bmatrix} 1 & -1 & 0 & 0 & 0 & 0 \\ 0 & 1 & -1 & 0 & 0 & 0 \\ 0 & 0 & 1 & -1 & 0 & 0 \\ 0 & 0 & 0 & 1 & -1 & 0 \\ 0 & 0 & 0 & 0 & 1 & -1 \\ 0 & 0 & 0 & 0 & 0 & 1 \end{bmatrix}. \tag{12}$$

The non-negative component of Assumption **A4** sets $\theta_{lower} = 0$ and leaves θ_{upper} unbounded and the conservation of volume component is enforced by the selection of

$$\mathbf{A}_e = \begin{bmatrix} \mathbf{0}^{1\times 6} & 1 & 4 & 4 & 4 & 8 & 4 \end{bmatrix}; \mathbf{B}_e = 1. \tag{13}$$

The non-zero elements in $\mathbf{A}_e$ indicate the counts that the corresponding parameter appears in h_g (e.g. h_{g_1} appears 1 time and h_{g_5} appears 8 times in h_g from **A1.** and **A2.**. The construction of h_f and h_g is shown in Fig. 8.)

V. SYSTEM IDENTIFICATION RESULTS

A. Nominal models

Nominal models for h_f and h_g were obtained as described in Section IV-B. The identified $5\times$ 5 h_f matrix has all nonzero elements, and its central element value is 14% of the sum of all 25 element values, shown in Fig. 9. The spatial dispersion of the identified h_f is indicated by its weighted standard distance (Appendix II) of 1.7 pixel pitches (8.5 μm) from the matrix center. This mass transport beyond the central pixel consistent with coalescence of viscous, densely packed drops [14]. The identified h_g, however, has no spatial dispersion, as shown in Fig. 10, indicating the material at the previous layer almost perfectly maps to material addition in the second layer. This behavior ideal and means that layer-to-layer dynamics act like a pure integrator; this result confirms our expectation introduced in Remark 1.

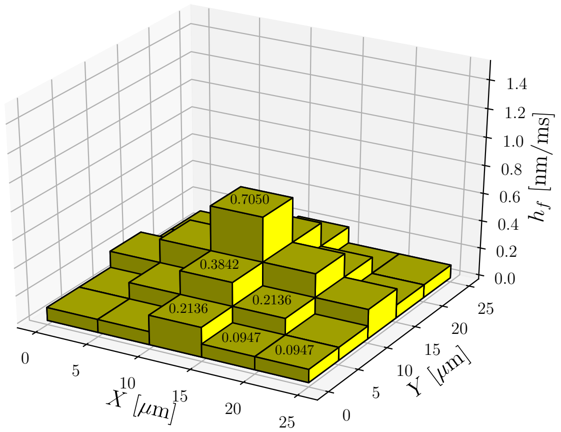

Fig. 9. Nominal h_f model obtained via system identification.

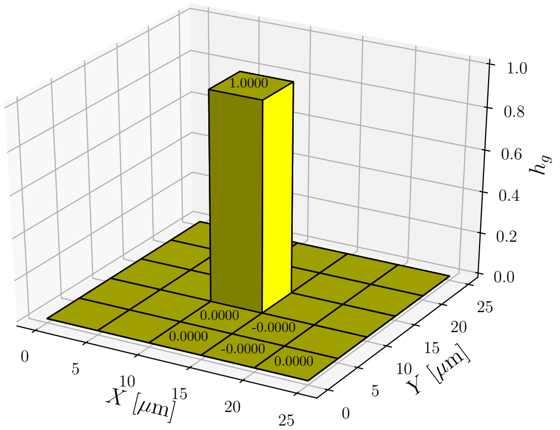

Fig. 10. Nominal h_g model obtained via system identification. The negative signs are caused by the software numerical precision.

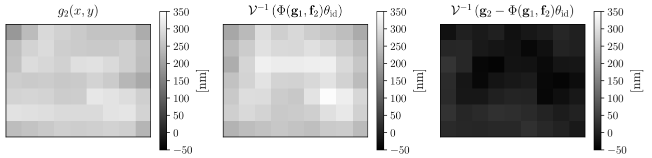

Fig. 11. Worst case prediction error from the validation set, as defined in (14).

B. Model validation

The error metrics as defined in (9) are compared to quantitatively evaluate the models. The values of $E^{\text{exp}}_{\text{rms}}$ and $E^{\text{val}}_{\text{rms}}$ are presented in Table I. The values of $E^{\text{exp}}_{\text{rms}}$ and $E^{\text{val}}_{\text{rms}}$ are close to each other. $E^{\text{val}}_{\text{rms}}$ is 3.6% smaller than $E^{\text{exp}}_{\text{rms}}$.

TABLE I

ERROR METRICS (UNIT: μM)

$E^{\text{exp}}_{\text{rms}}$	$E^{\text{val}}_{\text{rms}}$
0.0386	0.0372

A more visual model evaluation is presented in Fig. 11. The figure presents the worst-case topography height prediction of the validation run out of 10 runs,

$$\max_i \|\mathbf{g}_2 - \Phi(\mathbf{f}_2, \mathbf{g}_1)\theta_{\text{id}}\|_2, \tag{14}$$

where i is the run index, $\mathbf{f}_2 = \mathcal{V}\left(d_i \bar{\bar{f}}_2\right)$ is the input and $\mathbf{g}_{(\cdot)}$ is the corresponding output. Qualitatively, the model error is a fraction of the model parameter values.

VI. CONCLUSIONS

This manuscript describes a system identification method to define a discrete spatial repetitive process model for microscale additive manufacturing. The identified model accurately represents both the in-layer and layer-to-layer dynamics of electrohydrodynamic jet printing, demonstrated by a less than 4% error between the training set data and the validation data using a different input. Note that the system identification routine used a pseudo random binary sequence input signal, hence exciting the system with a broad-band of frequencies, and also used multiple input magnitudes, and thus may have excited nonlinearities in the system that are not captured by our linear discrete repetitive process model. Future work will investigate the extensibility of this model to other material systems used with electrohydrodynamic jet printing and investigations using the identified models in model-based controllers to regulate part topograpy in multi-layer and multi-material fabrication.

APPENDIX I: FORMULATION OF $\Phi(\mathbf{f}_{j+1}, \mathbf{g}_j)$

This section provides the derivation to obtain $\Phi(\mathbf{f}_{j+1}, \mathbf{g}_j)$. The element in the u-th row and the v-th column of Φ is written as $\Phi[u, v]$. From (4) and linear algebra, the following relation can be obtained,

$$\mathbf{g}_{j+1}[u] = \sum_{v=0}^{2(2M-1)(2N-1)-1} \Phi[u,v]\theta[v], \tag{15}$$

where $\mathbf{g}_{j+1}[u]$ is the u-th element of vector $\mathbf{g}_{j+1}$, and $\theta[v]$ is the v-th element of θ. From the definition of the vectorization operator $\mathcal{V}$ [15], $\mathbf{g}_{j+1}[u]$ can be written as $g_{j+1}(u_x, u_y)$, where

$$\begin{aligned} u_x &= \lfloor \frac{u}{N} \rfloor, \\ u_y &= u \bmod N. \end{aligned} \tag{16}$$

The notation $\lfloor \cdot \rfloor$ denotes the floor function. From (5), $\theta[v]$ can be written as $h_f(v_x, v_y)$ if $0 \leqslant v < (2M-1)(2N-1)$, or $h_g(v_x, v_y)$ if $v \geqslant (2M-1)(2N-1)$ where

$$\begin{aligned} v_x &= \lfloor \frac{v'}{2N-1} \rfloor + 1 - M, \\ v_y &= (v' \bmod 2N-1) + 1 - N, \end{aligned} \tag{17}$$

where $v' = v \bmod (2M-1)(2N-1)$. Therefore, (15) can be rewritten as

$$\begin{aligned} g_{j+1}(u_x, u_y) = & \sum_{v=0}^{(2M-1)(2N-1)-1} \Phi[u,v]\theta[v] \\ &+ \sum_{v=(2M-1)(2N-1)}^{2(2M-1)(2N-1)-1} \Phi[u,v]\theta[v] \\ &= \sum_{v=0}^{(2M-1)(2N-1)-1} \Phi[u,v]h_f(v_x, v_y) \\ &+ \sum_{v=(2M-1)(2N-1)}^{2(2M-1)(2N-1)-1} \Phi[u,v]h_g(v_x, v_y). \end{aligned} \tag{18}$$

From the commutative property of convolution, the system dynamics in (2) can be rewritten as

$$\begin{aligned} g_{j+1}(x,y) &= (f_{j+1} * h_f)(x,y) + (g_j * h_g)(x,y) \\ &= \sum_{u=1-M}^{M-1} \sum_{v=1-N}^{N-1} h_f(u,v) f_{j+1}(x-u, y-v) \\ &+ \sum_{u=1-M}^{M-1} \sum_{v=1-N}^{N-1} h_g(u,v) g_j(x-u, y-v), \end{aligned} \tag{19}$$

where

$$\begin{aligned} & f_{j+1}(x,y) = 0 \text{ and } g_j(x,y) = 0 \\ & \quad \text{if } x \notin \{0, 1, \ldots, M-1\} \text{ or } y \notin \{0, 1, \ldots, N-1\}. \end{aligned}$$

From (18) and (19),

$$\begin{aligned} \Phi[u,v] &= f_{j+1}(u_x - v_x, u_y - v_y) \\ & \quad \text{if } 0 \leqslant v < (2M-1)(2N-1); \\ \Phi[u,v] &= g_j(u_x - v_x, u_y - v_y) \\ & \quad \text{if } v \geqslant (2M-1)(2N-1). \end{aligned} \tag{20}$$

Equivalently, (20) can be written as

$$\begin{aligned} \Phi[u,v] = & \left(1 - \lfloor \frac{v}{(2M-1)(2N-1)} \rfloor \right) \\ & \times f_{j+1}(u_x - v_x, u_y - v_y) \\ & + \lfloor \frac{v}{(2M-1)(2N-1)} \rfloor \times g_j(u_x - v_x, u_y - v_y). \end{aligned} \tag{21}$$

The universal formulation of $\Phi[u, v]$ can be obtained by substituting (16) and (17) into (21):

$$\begin{aligned} & \Phi[u,v] \\ = & \left(1 - \lfloor \frac{v}{(2M-1)(2N-1)} \rfloor \right) \\ & \times f_{j+1}\{\lfloor \frac{u}{N} \rfloor - \left(\lfloor \frac{v'}{2N-1} \rfloor + 1 - M \right), \\ & (u \bmod N) - ((v' \bmod 2N-1) + 1 - N)\} \\ & + \lfloor \frac{v}{(2M-1)(2N-1)} \rfloor \\ & \times g_j\{\lfloor \frac{u}{N} \rfloor - \left(\lfloor \frac{v'}{2N-1} \rfloor + 1 - M \right), \\ & (u \bmod N) - ((v' \bmod 2N-1) + 1 - N)\}. \end{aligned}$$

APPENDIX II: COMPUTATION OF WEIGHTED STANDARD DISTANCE OF A SQUARE MATRIX

Let $A \in \mathbb{R}^2$ be a square matrix of size N with elements $a_{i,j} \forall (i,j) \in \{0, 1, ..., N-1\} \times \{0, 1, ..., N-1\}$. The x position x_i and y position y_j of element $a_{i,j}$ are $\frac{i+1}{2}$ and $\frac{j+1}{2}$, respectively, relative to the top left corner of the matrix. The weighted mean x and y positions $\bar{x}$ and $\bar{y}$ of the matrix are

$$\bar{x} = \frac{\sum_{i=0}^{N-1}\sum_{j=0}^{N-1} a_{i,j}x_i}{\sum_{i=0}^{N-1}\sum_{j=0}^{N-1} a_{i,j}}, \quad \text{and} \tag{22}$$

$$\bar{y} = \frac{\sum_{i=0}^{N-1}\sum_{j=0}^{N-1} a_{i,j}y_j}{\sum_{i=0}^{N-1}\sum_{j=0}^{N-1} a_{i,j}}. \tag{23}$$

The weighted standard distance of the matrix is

$$\left(\frac{\sum_{i=0}^{N}\sum_{j=0}^{N} a_{i,j}\left((x_i-\bar{x})^2+(y_i-\bar{y})^2\right)}{\frac{N^2-2}{N^2}\sum_{i=0}^{N}\sum_{j=0}^{N} a_{i,j}}\right)^{\frac{1}{2}}. \tag{24}$$

REFERENCES

[1] I. Gibson, D. Rosen, and B. Stucker, *Additive manufacturing technologies: 3D printing, rapid prototyping, and direct digital manufacturing*. Springer, 2014.

[2] J. Park, M. Hardy, S. J. Kang, K. Barton, K. Adair, D. Mukhopadhyay, C. Y. Lee, M. S. Strano, A. G. Alleyne, J. G. Georgiadis, P. M. Ferreira, and J. A. Rogers, "High-resolution electrohydrodynamic jet printing," *Nature Materials*, vol. 6, pp. 782–789, 2007.

[3] J.-U. Park, J. H. Lee, U. Paik, Y. Lu, and J. A. Rogers, "Nanoscale patterns of oligonucleotides formed by electrohydrodynamic jet printing with applications in biosensing and nanomaterials assembly," *Nano letters*, vol. 8, no. 12, pp. 4210–4216, 2008.

[4] M. S. Onses, C. Song, L. Williamson, E. Sutanto, P. M. Ferreira, A. G. Alleyne, P. F. Nealey, H. Ahn, and J. A. Rogers, "Hierarchical patterns of three-dimensional block-copolymer films formed by electrohydrodynamic jet printing and self-assembly," *Nature nanotechnology*, vol. 8, no. 9, pp. 667–675, 2013.

[5] S. Lee, J. Kim, J. Choi, H. Park, J. Ha, Y. Kim, J. A. Rogers, and U. Paik, "Patterned oxide semiconductor by electrohydrodynamic jet printing for transparent thin film transistors," *Applied physics letters*, vol. 100, no. 10, p. 102108, 2012.

[6] S. Jeong, J.-Y. Lee, S. S. Lee, Y.-H. Seo, S.-Y. Kim, J.-U. Park, B.-H. Ryu, W. Yang, J. Moon, and Y. Choi, "Metal salt-derived in–ga–zn–o semiconductors incorporating formamide as a novel co-solvent for producing solution-processed, electrohydrodynamic-jet printed, high performance oxide transistors," *Journal of Materials Chemistry C*, vol. 1, no. 27, pp. 4236–4243, 2013.

[7] D. Lee, J. Lee, P. S. Shin, Y.S., Y. Yu, Y. Kim, and J. Hwang, "Structuring of conductive silver line by electrohydrodynamic jet printing and its electrical characterization," *Journal of Physics: Conference Series*, vol. 142, p. 012039, 2008.

[8] S. Jayasinghe, A. Qureshi, and P. Eagles, "Electrohydrodynamic jet processing: An advanced electric-field-driven jetting phenomenon for processing living cells," *Small*, vol. 2, no. 2, pp. 216–219, 2006.

[9] S. Chung, J. R. Felts, D. Wang, W. P. King, and J. J. De Yoreo, "Temperature-dependence of ink transport during thermal dip-pen nanolithography," *Applied Physics Letters*, vol. 99, no. 19, 2011.

[10] J.-U. Park, S. Lee, S. Unarunotai, Y. Sun, S. Dunham, T. Song, P. M. Ferreira, A. G. Alleyne, U. Paik, and J. A. Rogers, "Nanoscale, electrified liquid jets for high-resolution printing of charge," *Nano Letters*, vol. 10, no. 2, pp. 584–591, 2010.

[11] P. M. Sammons, D. A. Bristow, and R. G. Landers, "Height Dependent Laser Metal Deposition Process Modeling," *Journal of Manufacturing Science and Engineering*, vol. 135, no. 5, p. 054501, Sep. 2013.

[12] L. Lu, J. Zheng, and S. Mishra, "A layer-to-layer model and feedback control of ink-jet 3-d printing," *IEEE/ASME Transactions on Mechatronics*, vol. 20, no. 3, pp. 1056–1068, 2015.

[13] D. J. Hoelzle and K. L. Barton, "On spatial iterative learning control via two dimensional convolution: Stability analysis and computational efficiency," *IEEE Trans. on Control Systems Technology*, vol. 24, no. 4, pp. 1504–1512, 2016.

[14] Z. Wang, C. Pannier, L. Ojeda, K. Barton, and D. J. Hoelzle, "An application of spatial iterative learning control to micro-additive manufacturing," in *2016 American Control Conference (ACC)*. IEEE, 2016, pp. 354–359.

[15] R. C. Gonzalez and P. Wintz, *Digital Image Processing*, 1st ed. Addison-Wesley, 1977.

[16] T. Söderström and P. G. Stoica, *System Identification*. Prentice Hall, 1989.

[17] R. Pintelon and J. Schoukens, *System identification: a frequency domain approach*. John Wiley & Sons, 2012.

[18] F. J. MacWilliams and N. J. Sloane, "Pseudo-random sequences and arrays," *Proceedings of the IEEE*, vol. 64, no. 12, pp. 1715–1729, 1976.

[19] K. Wang and J. P. Stark, "Voltage effects on the nanoelectrospray characteristics in fully voltage-controlled atomisation of gold nanocolloids," *Analytica chimica acta*, vol. 679, no. 1, pp. 81–84, 2010.

[20] K. Wang and J. Stark, "Deposition of colloidal gold nanoparticles by fully pulsed-voltage-controlled electrohydrodynamic atomisation," *Journal of Nanoparticle Research*, vol. 12, no. 3, pp. 707–711, 2010.

[21] K. Wang, M. D. Paine, and J. P. Stark, "Fully voltage-controlled electrohydrodynamic jet printing of conductive silver tracks with a sub-100 μ m linewidth," *Journal of applied physics*, vol. 106, no. 2, p. 024907, 2009.

[22] S. Son, S. Lee, and J. Choi, "Fine metal line patterning on hydrophilic non-conductive substrates based on electrohydrodynamic printing and laser sintering," *Journal of Electrostatics*, vol. 72, no. 1, pp. 70–75, 2014.

[23] M. S. Onses, A. Ramírez-Hernández, S.-M. Hur, E. Sutanto, L. Williamson, A. G. Alleyne, P. F. Nealey, J. J. de Pablo, and J. A. Rogers, "Block copolymer assembly on nanoscale patterns of polymer brushes formed by electrohydrodynamic jet printing," *Acs Nano*, vol. 8, no. 7, pp. 6606–6613, 2014.

[24] J. H. Pikul, P. Graf, S. Mishra, K. Barton, Y.-K. Kim, J. A. Rogers, A. Alleyne, P. M. Ferreira, and W. P. King, "High precision electrohydrodynamic printing of polymer onto microcantilever sensors," *IEEE Sensors Journal*, vol. 11, no. 10, pp. 2246–2253, 2011.

[25] E. A. Corbin, L. J. Millet, J. H. Pikul, C. L. Johnson, J. G. Georgiadis, W. P. King, and R. Bashir, "Micromechanical properties of hydrogels measured with mems resonant sensors," *Biomedical microdevices*, vol. 15, no. 2, pp. 311–319, 2013.

[26] G. Arrabito and B. Pignataro, "Solution processed micro-and nano-bioarrays for multiplexed biosensing," 2012.

[27] M. S. Onses, P. Pathak, C.-C. Liu, F. Cerrina, and P. F. Nealey, "Localization of multiple dna sequences on nanopatterns," *Acs Nano*, vol. 5, no. 10, pp. 7899–7909, 2011.

[28] M. S. Onses, E. Sutanto, P. M. Ferreira, A. G. Alleyne, and J. A. Rogers, "Mechanisms, capabilities, and applications of high-resolution electrohydrodynamic jet printing," *Small*, vol. 11, no. 34, pp. 4237–4266, 2015.

[29] C. P. Pannier, L. Ojeda, Z. Wang, D. J. Hoelzle, and K. L. Barton, "An electrohydrodynamic jet printer with integrated metrology," *submitted to Mechatronics*.

[30] C. P. Pannier, M. Diagne, I. A. Spiegel, D. J. Hoelzle, and K. Barton, "A dynamic model of drop spreading in electrohydrodynamic jet printing," *Journal of Manufacturing Science and Engineering*, vol. 139, p. 111008, 2017.

[31] B. Widom, "Line tension and the shape of a sessile drop," *The Journal of Physical Chemistry*, vol. 99, no. 9, pp. 2803–2806, 1995.